UCRL 8865

UNIVERSITY OF
CALIFORNIA
Ernest O. Lawrence
Radiation Laboratory

ANTIPROTON-PROTON CROSS SECTIONS AT 1.0, 1.25, AND 2.0 Bev

BERKELEY, CALIFORNIA

DISCLAIMER

UCRL-8865
Physics and Mathematics
TID-4500-15th Ed.

UNIVERSITY OF CALIFORNIA

Lawrence Radiation Laboratory
Berkeley, California

Contract No. W-7405-eng-48

ANTIPROTON-PROTON CROSS SECTIONS AT 1.0, 1.25, AND 2.0 Bev

Charles A. Coombes
(Thesis)

March 15, 1960

Printed in USA. Price $1.50. Available from the
Office of Technical Services
U. S. Department of Commerce
Washington 25, D.C.

ANTIPROTON-PROTON CROSS SECTIONS AT 1.0, 1.25, AND 2.0 Bev

Contents

ANTIPROTON-PROTON CROSS SECTIONS AT 1.0, 1.25, AND 2.0 Bev

Charles A. Coombes

Lawrence Radiation Laboratory
University of California
Berkeley, California

March 15, 1960

ABSTRACT

The antiproton-proton interaction was studied at three energies, 2.0, 1.25 and 0.98 Bev. Antiprotons produced internally in the Bevatron and channeled externally by a system of bending magnets and quadrupoles were selected from background particles by using a gas Čerenkov counter and scintillation counters. At the two lower energies, an electrostatic-magnetic velocity spectrometer was used to reject background particles. A liquid-hydrogen target was completely surrounded by scintillation counters so that all charged secondaries from the antiproton-proton interactions could be detected. With the information obtained from these counters, the $\bar{P}$-P total, elastic, inelastic, and charge-exchange cross sections and the angular distribution of the elastic scatterings were obtained at each energy. The total cross section was found to be 80, 89, and 100 mb at 2.0, 1.25, and 0.98 Bev, respectively. The inelastic cross section was about two-thirds of the total cross section at each energy. It was found that each of the partial cross sections was dropping off slowly with energy. The results were fitted by an optical-model calculation.

INTRODUCTION

A detailed study of the antiproton-proton interaction at high energies can yield considerable information about the structure of the nucleon as well as more knowledge about nuclear forces. In the experiment described here, antiproton-proton cross sections were measured at 2.0 Bev. This energy is close to the highest energy practicable at the Bevatron if present time-of-flight methods are used, for the temporal separation of antiprotons from unwanted particles within a reasonable distance becomes increasingly small with energy. It is impossible to go to a much higher energy at the Bevatron by any method, since the yield of antiprotons decreases rapidly with increasing energy and is expected to become zero at about 3 Bev.

Measurements of the cross sections were also made at 0.98 and 1.25 Bev. The cross sections were measured at 0.98 Bev in order to be able to directly compare the results of this experiment with those of a similar experiment carried out earlier. The third run was made at 1.25 Bev to help fill in the cross-section energy curves. A fourth run had been planned between 1.25 and 2 Bev, but this could not be done in the Bevatron time allotted.

Following the discovery of the antiproton,[1] several experiments were done[2,3,4,5] in which it was observed that antiprotons interacted much more strongly with nuclei than protons did.

The first measurements of the antiproton-proton cross sections were done by Cork et al.[6] in the energy range of 190 to 700 Mev. The results of this experiment, which was done using a 5-ft hydrogen target and good geometry, were that the antiproton-proton total cross section was about twice the proton-proton total cross section. These results were followed by those of Chamberlain et al. who measured the antiproton-proton inelastic cross section at 450 Mev.[7] They used a Čerenkov counter as a target and a difference method ($H_2O - \frac{1}{2} O_2$) to calculate the antiproton-proton inelastic cross section.

The geometry was such that scatterings at angles smaller than 14 deg could not be measured. The inelastic cross section obtained by Chamberlain et al.[7] was about the same size as the total cross section obtained by Cork et al.[6] for a similar energy. Either the elastic-scattering cross section was very small or an error had been made in one of the experiments. It has since been shown that the elastic-scattering cross section is a substantial part of the total cross section. Therefore, there is discrepancy between the results of Cork et al. and Chamberlain et al. Recently Elliof et al. completed an experiment which measured the cross sections at the same energy.[8] If their results are correct, the total cross section measured by Cork et al. was low, and the results of Chamberlain et al. were high.

Measurements of the elastic antiproton proton cross section which showed that elastic scattering was a large fraction of the total cross section were made by Agnew et al.,[9] Goldhaber et al.,[10] and Coombes et al.[11] The results of Coombes et al. also gave the total and partial (inelastic, charge-exchange, and elastic) cross sections in the energy range from 133 to 333 Mev. The angular distributions of the elastic scatterings were also obtained, and it was shown that the antiprotons were scattered mainly in the forward direction. These results indicated a strongly absorptive interaction with a radius of the order of 1.5×10^{-13} cm.

Two of the theoretical attempts to explain the antiproton-proton interaction are in good agreement with the above-mentioned experimental results. One is the model of Ball and Chew, who used the Yukawa formalism and a potential that correctly describes the nucleon-nucleon interaction to calculate the different partial cross sections.[12] They assumed that the annihilation interaction is caused by the short-range absorbing core--a nucleon is considered to be a complex structure consisting of a central core surrounded by a pion cloud. Each partial wave that gets through the centripetal barrier is assumed to be attracted to the core and absorbed. Because the WKB

approximation was used to calculate the phase shifts and to estimate the probability of absorption of each partial wave, the method could not be used above about 200 Mev. Fulco used the phase shifts calculated by Ball and Chew to calculate the angular distributions of the elastic scattering at 140 and 260 Mev.[13]

The second theory that is in good agreement with experiment is one advanced by Koba and Takeda.[14] They used approximately the same model of interaction as that of Ball and Chew, but took a much more phenomenological approach. While the results of Ball and Chew are limited to low energies, the results of Koba and Takeda are much more general and apply over a wide range of energies. Their model will be discussed in the Conclusion and compared with the results of the experiment described in this paper.

ANTIPROTON BEAM

The antiprotons were produced internally in the Bevatron by the primary proton beam and bent into the external magnet channel by the Bevatron field (see Fig. 1). The radiofrequency structure of the proton beam of the Bevatron was removed by making the beam pass through a thin foil which caused the protons to lose a small amount of their energy.[6] This loss made the proton beam phase-unstable, and as a result the beam spiraled into the target. By this technique, the secondary beam was produced uniformly over a period of 50 milliseconds. A different target was used at each momentum. These targets were located so that the negative particles selected by the external system came off the target in the forward direction. As a result, the antiproton yield was at a maximum, and the apparent source size was a minimum. The targets were 1/2-in. by 3/8-in. by 6 in. and were made of beryllium.

After emerging from the Bevatron, the negative beam was steered into the following 8-in. aperture quadrupole, Q_1, by a deflecting magnet, C_1. By use of the magnet C_1 and by use of different targets for each energy, it was possible to change momentum without changing the position of the external magnet system. In the vertical plane, quadrupole Q_1 focused the beam from the target on a 2-in. slit at the entrance to magnet M, while in the horizontal plane it focused the beam on an 8-in. collimator (not shown in Fig. 1) at the entrance to the quadrupole set Q_2. Quadrupole Q_1 was placed as close to the target as possible in order to obtain the maximum solid angle of acceptance. The momentum spread in the beam, about ±6%, was determined by the width of the horizontal collimator and the dispersion produced by the Bevatron field.

After Q_1, the beam passed though a 40ft-long velocity spectrometer of the parallel-plate type.[11] Crossed electric (E) and magnetic fields (H) allowed particles of a certain velocity (β_0=E/H)

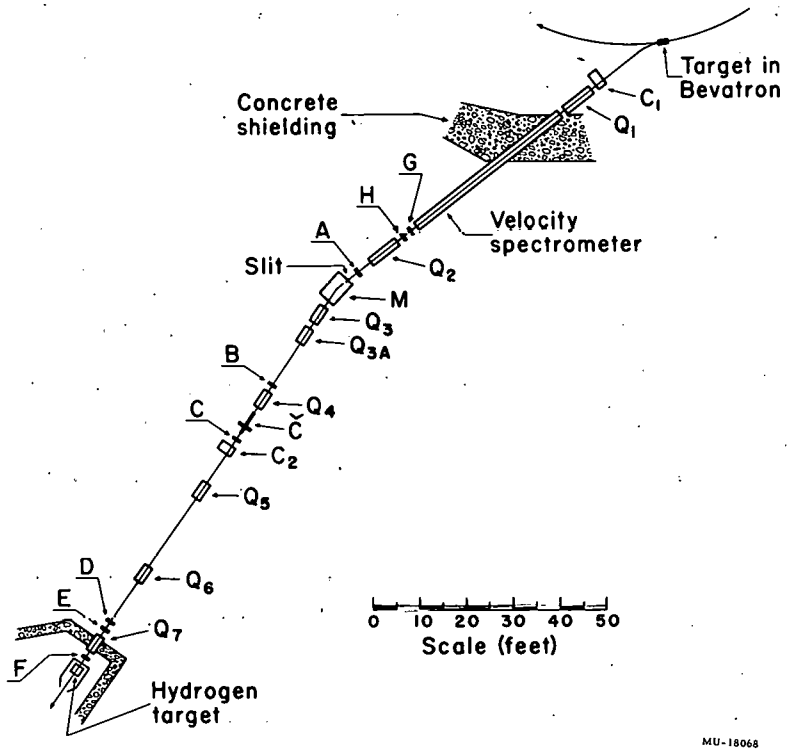

Fig. 1. Experimental arrangement. Here C_1, C_2 and M are deflecting magnets. Quadrupole sets Q_1 and Q_2 have 8-in. apertures; Q_3-Q_7 have 4-in. apertures Counters A through F are 4-by 4-by 1/4-in. plastic scintillators used for time-of-flight measurement. Counters G and H were 4-by 8-by 1/4-in.

to pass through with no deflection since the electric and magnetic forces just canceled each other. Particles with different velocities were deflected either up or down. The spectrometer was set to give no deflection to the antiprotons, while faster particles (π mesons, K mesons) were deflected vertically by an amount that depended on their momentum, p, as shown by the relationship

$$y = \frac{e\ell^2 E}{2cp}\left(\frac{1}{\beta_0} - \frac{1}{\beta}\right), \qquad (1)$$

where y is the distance deflected (measured at the exit of the spectrometer and neglecting second-order terms), β is the velocity of the particle whose charge is e, and ℓ is the effective length of the spectrometer. Most of the faster particles struck the upper edge of the slit at the entrance to M and were absorbed or degraded sufficiently so that they were removed from the beam by the deflecting magnet M. The spectrometer was used at 1.7 Bev/c and 2.0 Bev/c but not at 2.8 Bev/c, since at this momentum the amount the fast particles were deflected was small compared to the beam width.

In the horizontal plane, the quadrupole Q_2 acted as a field lens, redirecting particles of different momenta toward the center of the deflecting magnet M. Magnet M accurately determined the average momentum selected and undid most of the dispersion created by the Bevatron field. Thus, it was able to direct the particles of different momenta along the axis of the following iterated 4-in.-aperture quadrupole system (Q_3 to Q_7).

The transition (without appreciable beam loss) from the 8-in. to the 4-in. quadrupole system was aided by several factors. Canceling the momentum dispersion at the deflecting magnet M minimized the horizontal aperture required beyond that point, but in order to reduce the horizontal angular spread sufficiently, the 4-in. quadrupole Q_{3A} was necessary. Since the product of the angular spread of the beam and the width of the beam is a constant by

Liouville's theorem, the beam width in the horizontal direction was increased by Q_{3A}. The increase did not reduce the transmission of the system. The angular spread in the vertical direction was reduced by the focusing in M and in Q_{3A}.

The 4-in. lenses were spaced as close as possible to permit the transmission of particles with rather large angular divergences, but the over-all length had to be sufficiently long so that the antiprotons could be identified by time-of-flight. As a compromise between these two conflicting requirements, a length of 88 ft was chosen for the 4-in. system.

The bending magnet C_2 deflected the beam slightly in order to eliminate positive charged protons produced by collisions of the mesons in the beam with protons in the walls of the quadrupole and the Čerenkov counter. At the hydrogen target, the beam cross section was about 2 by 2 in.

ANTIPROTON YIELD AT THE BEVATRON

Table I gives the yield of antiprotons, π mesons, and K mesons measured at the end of the magnet channel. No corrections have been made for coulomb scattering or decay in flight. For the K's the fraction that decayed in flight is given in the last column. Some of the particles counted as K's could have been decay products that decayed at such a small angle that they were transmitted by the magnet system. This number was small, since the energy available in the center of mass is large for most of the decay products, and the products can come out at large angles. For pions, the number of decays in which the decay product is accepted by the system was large, since there is very little center-of-mass energy available to the muons.

The solid curve in Fig. 2 comes from a phase-space calculation for the yield of antiprotons from 6.1-Bev protons on protons and from 6.1-Bev protons on neutrons:[15]

$$P + P \rightarrow \bar{P} + P + P + P \qquad (2)$$

$$P + N \rightarrow \bar{P} + P + P + N . \qquad (3)$$

Table I

Beam characteristics. The momentum band width was ±6%. All quantities except P (protons striking the target) were measured at the exit of the magnet channel and correspond to operation with the spectrometer off. No corrections have been made for decay in flight. Operation of the spectrometer at 360kv rejects fast particles by the factor shown.

Average momentum (±3%) (Bev/c)	Solid angle (10^{-3} sterad)	$\bar{P}/P$ (10^{-12} ± 40%)	π^-/P (10^{-6} ±40%)	$\bar{P}/\pi^-$ (10^{-6})	K^-/π^- (±40%)	Spectrometer rejection factor (±30%)
1.7	0.40	60	1.3	45±5	0.028	3
2.0	0.33	60	1.2	48±5	0.015	2
2.8	0.50	15	0.9	15±5	0.009	-

The curve represents the yield of antiprotons per incident proton on the target, per unit momentum spread, and per acceptance solid angle. This curve is the sum of the curves for reactions (2) and (3) given by Fulco[13] with the exception that the yield given by Fulco has been weighted according to the momentum so that the yield is per momentum spread $\Delta p/p$ rather than per unit momentum interval (Δp). The experimental points in Fig. 2 are the number of antiprotons per pion measured in this and other experiments.[6, 11, 12] Differences in solid angles and in momentum spread between different experiments were compensated for by using the antiproton-pion ratio rather than the absolute yield of antiprotons, since the number of antiprotons and the number of pions both depend on these quantities in the same way. To compare the experimental points directly to the curve, we must correct the variation of the pion yield with momentum. Since the pion yield does not appear to change by more than a factor of three over the momentum range considered,[6, 8, 11] we can state that the phase-space calculation agrees with the experimental results within an order of magnitude. For some of the experimental points, the antiprotons were not produced in the forward direction. The curves for the yields at different angles given in reference 13 were used to normalize these points to the production curve in the forward direction. Only experiments that measured the yield at several momenta were considered, for in this way systematic errors would show up.

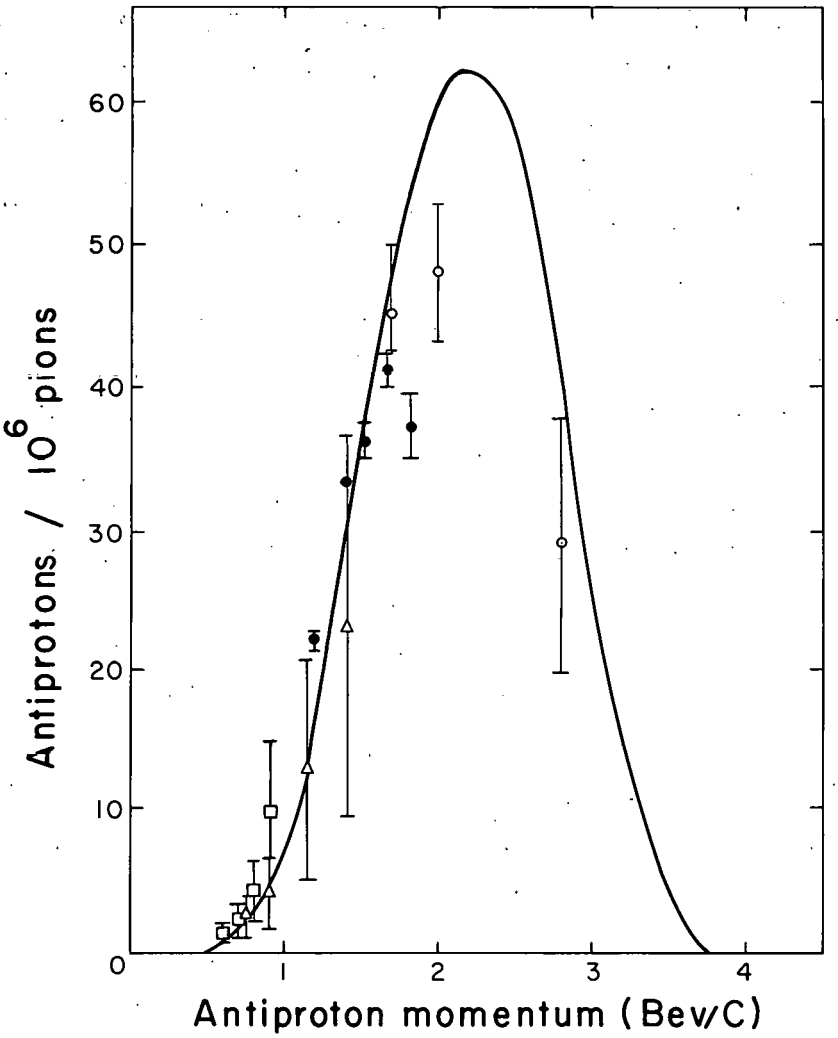

Fig. 2. The number of antiprotons produced relative to the number of pions produced at different momenta. The open circles are the results of this experiment. The solid circles are results of reference 8, squares reference 11, and triangles reference 6. The solid curve is the result of a phase-space calculation by Chamberlain et al. (Nuovo cimento 3, 447 (1956).

GAS ČERENKOV COUNTER

Since there were from 10,000 to 100,000 pions for each antiproton, a gas Čerenkov counter was used to help distinguish the antiprotons from the pions. Figure 3 shows a cross-sectional cut of it. It was made of an pion pipe 6-ft long by 5-in. diam. The interior of the pipe was lined with highly reflecting anodized aluminum. In the center of the cross were two plane mirrors which reflected the Čerenkov light into lenses in each arm of the cross. Each of these lenses focused light from the mirror onto an RCA 6810A photomultiplier. The output pulses of the two photomultipliers were added to give one output pulse.

Because methane has a low Z (and thus, does not cause much coulomb scattering) and because it has a fairly high index of refraction, it was used in the counter. The counter was tested at pressures up to 400 psi although in this experiment the counter was run at 200 psi. At this pressure the index of refraction is 1.0060 , which corresponds to a minimum β of 0.994. Particles with velocities less than 0.994 did not count in the counter, while particles with higher velocities did. A 1.2-Bev/c pion has this velocity; thus, in this experiment all pions and particles whose masses are less than that of the pion were counted by the counter.

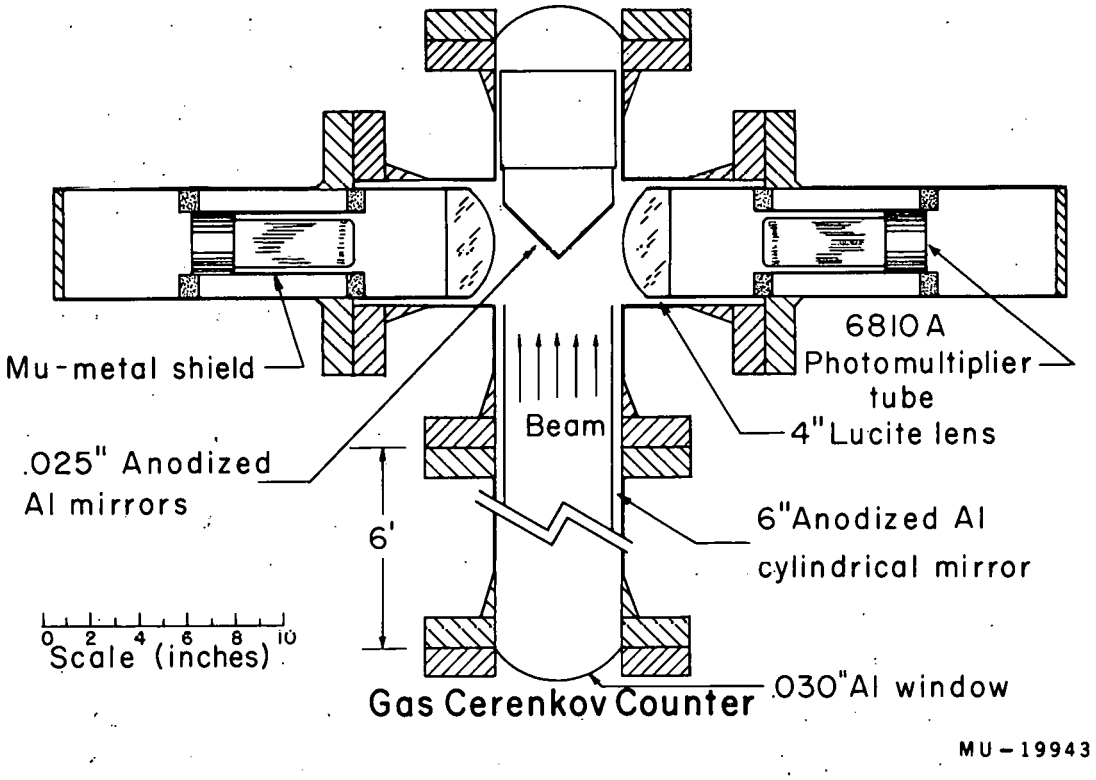

Fig. 3. Diagram of construction of the Gas Cerenkov counter.

HYDROGEN TARGET

A thin-walled liquid-hydrogen target[11] was used in the cross-section measurements (see Fig. 4). The hydrogen flask was of 0.010-in.-thick stainless steel, 12 in. long and 6 in. in diameter. In the evacuated space surrounding the flask was a thin (0.003-in) copper heat shield held at liquid-nitrogen temperature. The outer vacuum wall, at room temperature, was made thin over a large solid angle in the forward direction, so that antiprotons scattered at angles up to 60° in the laboratory system could escape without passing through much material. Finally, the target was constructed in such a way that scintillation counters could surround the whole structure.

ELECTRONICS

Figure 5 shows a block diagram of the electronics used at 2.8 Bev/c; the electronics at the other momenta were similar. The antiprotons were distinguished from the background particles by means of three fast (resolution of 2×10^{-9} seconds) triple-coincidence units whose output pulses were mixed together in a slow (resolution of 10^{-7} sec) triple-coincidence unit. In two of the fast units, C_1 and C_2, the time-of-flight counters (1/4-by 4-by 4-in. plastic scintillators with RCA C7264 tubes) were approximately equally spaced over a 120-ft distance (see Figs. 1 and 4). These units had a good rejection against two particle accidentals, since two pions going through two of the counters at the right time to simulate an antiproton would not go through the third counter at the right time. They also had a good rejection against a single fast particle being considered as an antiproton, since the distance between counters was large enough to distinguish the antiprotons from the other particles. The third unit, C_3, had one counter at the front of the 4-in. system and two at the end. Because the distance between the

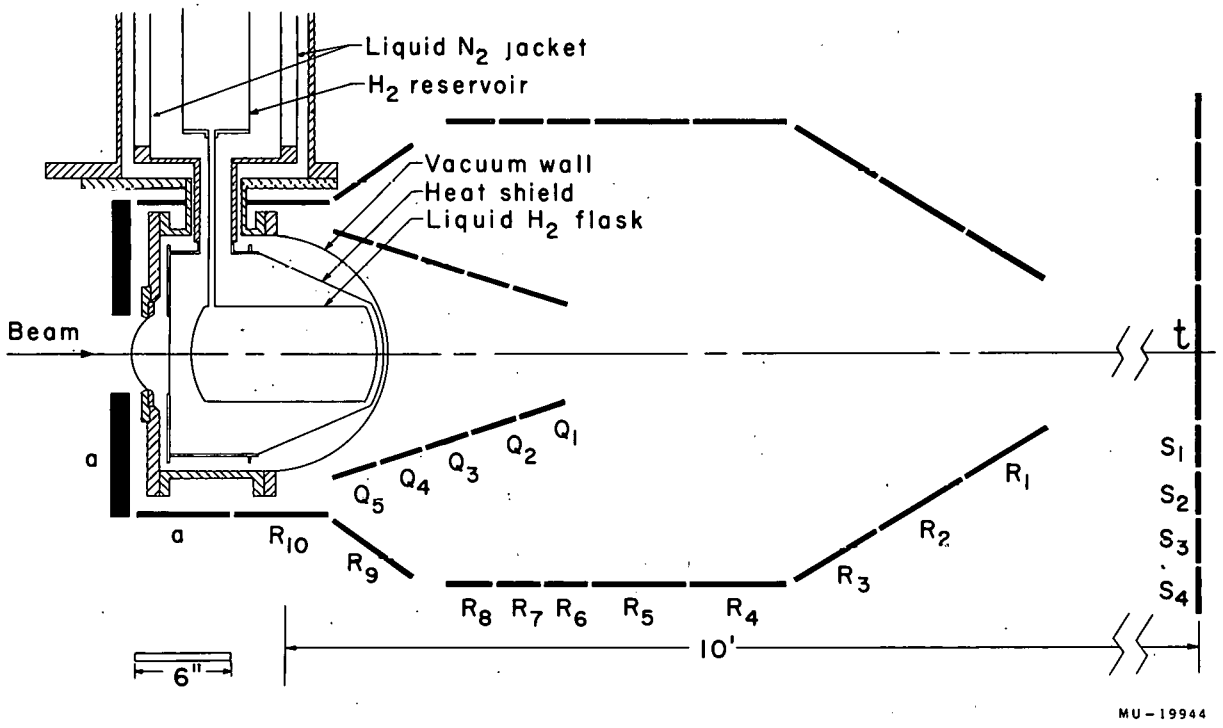

Fig. 4. Liquid-hydrogen target and surrounding counters. The target flask of 0.010-in. stainless steel was surrounded by a 0.003-in. copper heat shield and a 0.040-in. aluminum wall in the forward direction (gasket details are not shown). Counters $\underline{a}$, $\underline{t}$, $\overline{Q_1}$ through $\overline{Q_5}$, R_1 through R_{10}, and $\overline{S_1}$ through $\overline{S_4}$ were plastic scintillation counters. The lead was used to convert γ-rays from π^0 mesons.

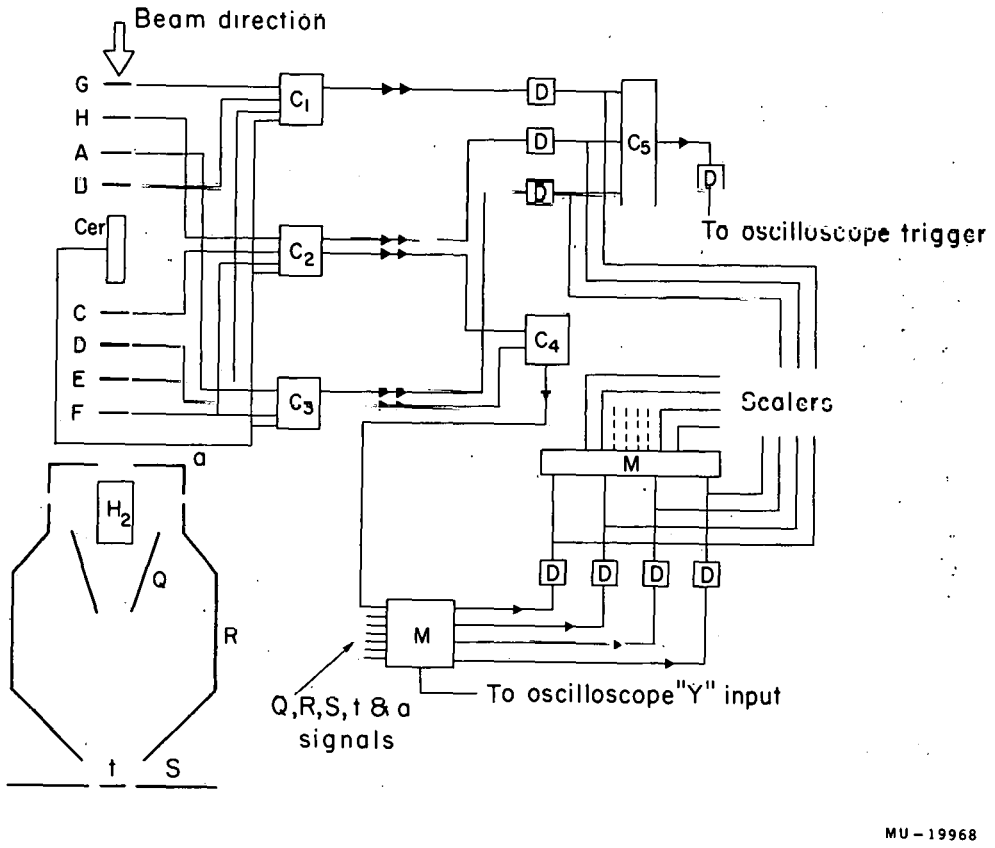

Fig. 5. Block diagram of basic electronics used at 2 Bev. A through H are time-of-flight scintillation counters; a, t, Q, R, and S are scintillation counters that detected the interactions of antiprotons in hydrogen; C_1 through C_5 are coincidence circuits; D's are discriminators; the triangles are amplifiers; M is a multichannel circuit in which individual counter pulses were mixed for display on an oscilloscope; and M' is a many-channel circuit in which sum signals from the different groups of counters were mixed.

first counter and the last two counters was quite large, this unit had a very good rejection against single fast particles. It was subject to twofold accidentals, since one particle going through the last two counters and another going through the first counter could simulate an antiproton. The gas Čerenkov counter was used in anticoincidence in each of the units. The outputs of these units were sent to discriminators and pulse shapers and then to the slow triple-coincidence unit. The output of the slow unit triggered an oscilloscope and a scaler, and a pulse from it was considered to mean an antiproton had entered the target. At the lower momenta, the counters G and H were not used, because the distance from A to F was enough to identify the antiprotons. Also, only two fast triple-coincidence units were used.

The output of two of the fast triple-coincidence units were mixed together in a fast coincidence unit (resolution of 10^{-8} sec) in order to obtain a fast gate for each antiproton incident on the hydrogen target. A multichannel coincidence mixer, M, made coincidences between the fast antiproton gate and all the counters surrounding the hydrogen target. The 40 gated-counter signals were inserted at points along two transmission lines, and the signals from the two lines were added together with opposite polarity so that when the signals were displayed on a Tektronix-517A oscilloscope, positive and negative pulses alternately appeared. In order to have a reference pulse, the antiproton gate was displayed on the oscilloscope. It was also used to help distinguish accidentals since, in general, an accidental gate pulse was smaller than an antiproton gate pulse. The oscilloscope face was photographed on 35mm film moving at a constant rate. The vertical position of the oscilloscope trace was displaced a few millimeters after each trace so that as many as 10 antiprotons per Bevatron pulse could be photographed.

Mixer M' formed all the possible coincidences between sum signals of the different groups of counters, and the output of these

coincidences was sent to scalers. Thus, the operation of the counters and electronics was continuously monitored. Two monitors were used to provide a check on the steering of the primary proton beam and the magnet channel. One monitor consisted of a threefold counter telescope that looked at the internal target; it monitored the beam "spillout". A second coincidence between counters E and F monitored the channel flux.

TIME-OF-FLIGHT RESOLUTION

In Fig. 6 the number of coincidences measured is plotted as a function of the amount of cable delay between the first and last counters. The ordinate was normalized to a unit incident-pion flux. At 2.0 Bev/c, the K^--peak yield dropped off to a reasonably low level before the antiproton peak was reached. On the assumption that the K^- curve at 2.8 Bev/c continued to drop off with cable delay as the β curve did, and that it had the same general shape as at 2.0 Bev/c, the curve was extended as shown by the dotted line. Since the extension of the K^- curve is just over a factor of 100 below the peak of the $\bar{P}$ curve, the number of coincidences from particles other than antiprotons was taken to be less than 1% of the number of coincidences from $\bar{P}$. This fraction would produce an even smaller fractional error in the cross sections. The curve is narrower at 2.8 Bev/c than at 2.0 Bev/c since at 2.8 Bev/c the discriminators were set more critically.

The effectiveness of C_1, C_2, and C_3 can be seen from the curves. Counter C_3 levels off at large delays at its twofold accidental rate. This leveling off does not mean that C_3 did not contribute anything to the identification of the antiprotons; rather, many of the K mesons were rejected by C_3, but all of the K's were not rejected since sometimes a pion went through the first counter just at the right time for the combination of pion and K^- to simulate an antiproton.

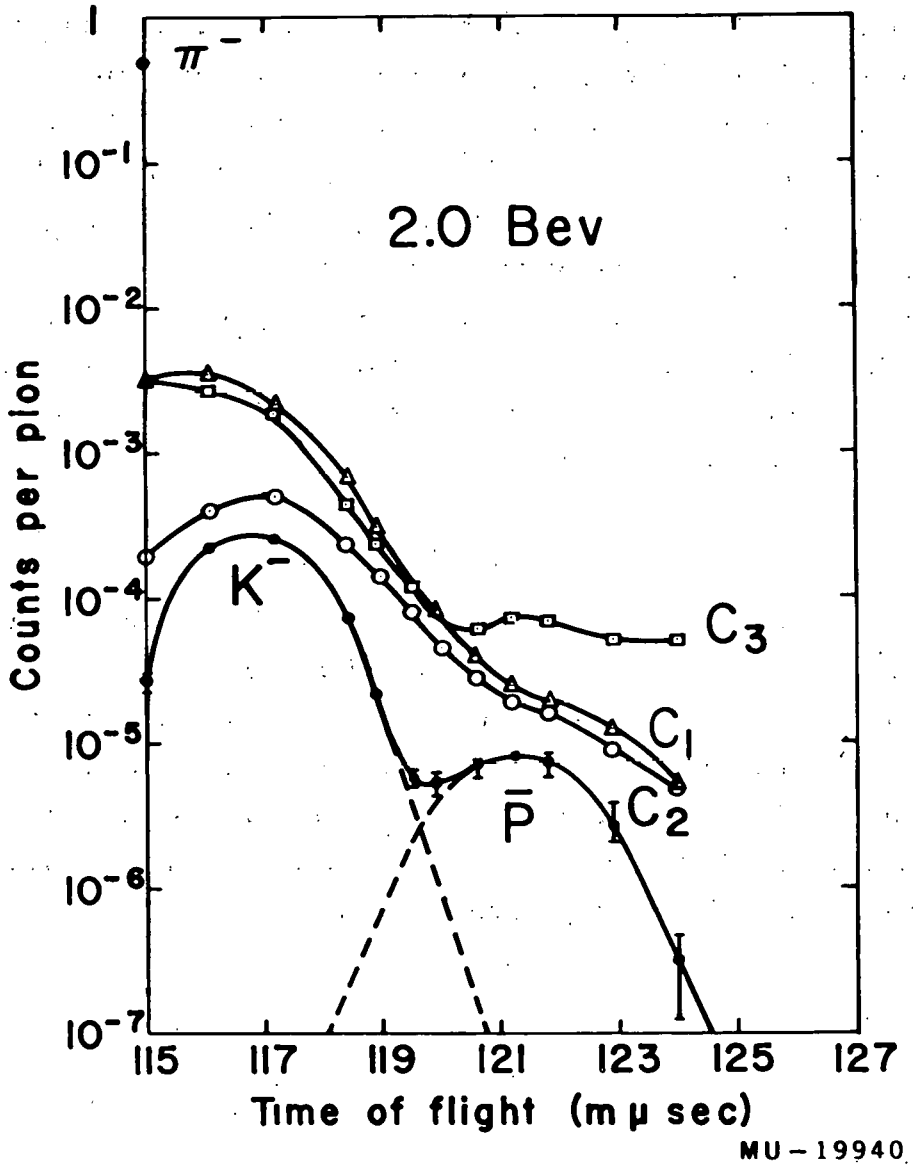

Fig. 6. Delay curve for time-of-flight counters at 2.8 Bev/c. The curves labeled C_1, C_2, and C_3 are outputs of threefold coincidence circuits. The bottom curve is a threefold coincidence between C_1, C_2, and C_3. The ordinate is normalized to the number of pions in the beam. The abscissa is the cable delay between G and F at 2.8 Bev/c. The point marked π^- indicates the fraction of the pions that were counted when the cable delay was set for pions.

An estimate of the efficiency of the gas Čerenkov counter can be obtained from the delay curves. When the gas counter was not used and the cable delay was such that the system was set to count pions, the point marked π^- was obtained. When the gas counter was used, the bottom point at 115 mμsec was obtained. This decrease in counting rate gives an efficiency of 99.99% for the gas counter. Since most, and maybe all, of the counts registered when the gas counter was used resulted from K mesons, the counter was really more efficient than 99.99%. Because of the Čerenkov counter, there were no background counts from pions when the system was tuned for antiprotons.

DATA REDUCTION

The scanning of the film was made faster and easier than in previous experiments by the use of an IBM card puncher.[6,11] Through use of the card puncher, the information contained on the photographs of the oscilloscope traces was transferred to IBM cards. The IBM cards were mechanically sorted into many different categories. Using the card puncher, a scanner could scan as many as 1000 antiproton events per hour.

DETECTION OF INTERACTIONS

The different types of antiproton-proton interactions that can take place are (a) elastic scatterings (b) inelastic scatterings (pion production) (c) annihilations, and (d) charge exchanges. To distinguish between these, one must consider many different things.

Since antiproton annihilations usually give off many charged and neutral secondaries, elastic scatterings can usually be distinguished from annihilations by observing the number of secondaries. To distinguish annihilations from inelastic scattering in which pions are produced is, in general, very difficult, since one must be able to determine whether or not an antiparticle is present in the secondaries.

Elastic scatterings can be distinguished by the fact that the two resulting particles are coplanar and have a definite angular relationship. Thus, for an event with two secondaries, one can determine whether or not it is a scattering by measuring the angles of the secondaries and measuring whether or not the two particles are coplanar with the incident particle.

Charge-exchanges can be distinguished from other events by ascertaining that no charged or neutral mesons are given off.

In this experiment, the hydrogen target was completely surrounded by plastic scintillation counters (see Fig. 4) so that the number of charged secondaries could be measured. Also, the counters were arranged in such a way that the angle of the secondaries was well defined. The counters were divided into five groups and labeled accordingly. All the counters were 1/4-in.-thick terphenyl-loaded polystyrene sheet with the exception of the a counter, which was 1-in. thick.

Since about one-third of the pions produced are neutral, a 1/2-in.-thick layer of lead was placed between the target and

counters R_9, R_{10}, and $\underline{a}$. This lead converted γ-rays from the neutral mesons ($\pi^0 \rightarrow 2\gamma$), thereby increasing the detection efficiency of the system for inelastic events. The thickness used was calculated to be the optimum for converting γ-rays without appreciably attenuating the charged particles. Lead was not used to all angles, as the material in the path of scattered antiprotons had to be kept small to minimize the number of scattered antiprotons that annihilated in the material surrounding the target.

The $\pm$ counter measured the fraction of the antiprotons transmitted, and corresponded to a good-geometry detector with which the total cross section could be measured.

Surrounding the $\pm$ counter were four ring counters called $\underline{s}$ which measured the small-angle differential-scattering cross section. For an event to be classified as a scattering into $\underline{s}$, one $\underline{s}$ counter and no other counters were seen. The exception to this rule was that pulses in $\underline{R}$ could occur with s_3 and s_4, since R overlapped $\underline{s}$. For scatterings into $\underline{s}$, the recoil protons were not seen as they did not have enough energy to get out of the target.

The angle subtended by the $\underline{a}$ counters was such that the only particles that could be detected by $\underline{a}$ were inelastic secondaries emitted backwards in the center of mass. Thus, all events with an $\underline{a}$ count were considered as inelastic events.

Through the use of the two sets of counters, Q and R, it was possible to define well the polar angle of the secondaries passing through the counters. Counter R was broken up into left and right zones, and Q was broken up into up and down zones. Thus, the quadrant through which any particle passed in going through Q and R was known.

The recoil protons were seen for antiprotons that scattered into $\underline{R}$. For an event with an $\underline{R}$ count to be classified as a scattering, the $\underline{Q}$ and $\underline{R}$ pulses had to be consistent with two

particles emerging. Moreover, the two particles had to go through opposite quadrants, and their measured angles had to be consistent with a scattering. If an event with observed secondaries did not fit the necessary requirements to be a scattering event it was considered to be an inelastic event.

Events for which no secondaries were observed were called misses and were considered to be charge exchanges.

CALCULATIONS, UNCERTAINTIES, AND CORRECTIONS

A. Total Cross Sections

The total cross section, σ_T, was obtained from the transmission with hydrogen in the target, t_i, and with hydrogen out, t_o, by

$$\sigma_T = \frac{1}{N_a} \ln \frac{t_o}{t_i} , \tag{4}$$

where N_a was the number of hydrogen atoms per square centimeter.

If one takes into account forward scattering into the transmission counter, t, the total cross section has to be increased by an amount

$$\Delta\sigma = \int (I^2 + R^2)\, d\Omega , \tag{5}$$

where I and R are, respectively, the imaginary and real parts of the forward scattering amplitude, and the integral is taken over the solid angle subtended by t at the target. If the amount of potential scattering is assumed to be small in comparison to the amount of diffraction scattering, then R should be small with respect to I, and R can be neglected in Eq. (5). Because the large-angle scattering cross section is small, and because the angular distribution is close to the black-disc distribution, the amount of potential scattering is probably small. Since the solid angle subtended by the t counter was small, no account was taken of the variation of I with angle. In this approximation Eq. (5) becomes

$$\Delta\sigma = I_0^2\, \Delta\Omega, \tag{6}$$

where I_0 is the imaginary part of the forward scattering amplitude and $\Delta\Omega$ is the solid angle of t at the target.

Using the "optical theorem",[16]

$$I_0 = \frac{\sigma_T}{4\pi\lambda} , \tag{7}$$

we obtain, from Eq. (6)

$$\Delta\sigma = \left(\frac{\sigma_T}{4\pi\lambda}\right)^2 \Delta\Omega , \tag{8}$$

where λ is the wave length of the incident antiproton in the center-of mass system.

B. Inelastic Cross Section

The inelastic cross section, σ_{in}, is given by:

$$\sigma_{in} = \frac{1}{N_a} \ell n \frac{t_{ao}}{t_{ai}} \tag{9}$$

where t_a is the fraction of the antiprotons that passed through the target without undergoing an inelastic collision. The subscripts i and o refer respectively to data taken with hydrogen in and out of the target.

Several effects have to be taken into account to obtain t_a from the experimentally observed numbers. This fraction is not simply given by

$$t_a = 1 - N_a , \tag{10}$$

where N_a is the fraction of antiprotons which were observed to produce inelastic events. Corrections have to be made for:

(a) the detection efficiency of (ϵ_a) of the counter system for inelastic events

(b) the fraction of observed inelastic events that were elastic scattered antiprotons that annihilated in counters and sent secondaries into other counters (thereby appearing as an inelastic event).

The factor t_a is given by

$$t_a = \frac{1 - N_a/\epsilon_a}{1 - \Sigma A_n S_n} , \tag{11}$$

where the term $\Sigma A_n S_n$ is fraction of the elastic scatterings that annihilated in the counters surrounding the hydrogen target.

C. Elastic Scattering Cross Section

The elastic-scattering cross section, σ_e, was given by

$$\sigma_e = \frac{1}{n_a} (S_i - S_0) , \qquad (12)$$

where

$$S = \sum_{\substack{\text{all} \\ \text{counters}}} s_n . \qquad (13)$$

Here s_n, the fraction of the antiprotons that would have scattered into the nth counter if that was the only process possible, is related to the measured fraction of antiprotons that scattered into the nth counter, N_{s_n}, by the relationship

$$s_n = \frac{N_{s_n} \left(1 + \frac{N_{s_n}}{2} + \sum_{\ell \geq n+1} N_{s_\ell}\right)}{t_a \epsilon_n (1-a_n)} . \qquad (14)$$

Here A_n is the fraction of the scatterings into the nth counter which annihilated, and ϵ_n is the detection efficiency of the nth counter.

The term t_a in Eq. (14) corrects for the fact that if an antiproton annihilated, it could not also have scattered into one of the counters, since it no longer existed. The term ϵ_n corrects for antiprotons that scattered through holes between the counters. The term $(1-a_n)$ corrects for the fraction of the scattered antiprotons that annihilated in the counters.

The term $\left(1 - \frac{N_{s_n}}{2} + \sum_{\ell \geq n+1} N_{a\ell}\right)$, which corrects for the thickness of the target, is in effect a plural scattering correction. The origin of this term can best be seen by considering a case where scattering is the only possible reaction. In that case, s_n is given by

$$s_n = N_{s_n} \left(1 + \frac{N_{s_n}}{2} + \sum_{\ell \geq n+1} N_{s\ell}\right) . \qquad (15)$$

and S is given by

$$S = \Sigma s_n = \Sigma \left\{ N_{sn} \left(1 + \frac{N_{sn}}{2} + \sum_{\ell \geq n+1} N_{s\ell} \right) \right\}$$

$$= N_S + \frac{N_S^2}{2} \qquad (16)$$

$$= N_S \left(1 + \frac{N_S}{2}\right) .$$

Thus, the scattering cross section is given by

$$\sigma_e = \frac{1}{N_a} \left\{ N_{Si} \left(1 + \frac{N_{Si}}{2}\right) - N_{So} \left(1 + \frac{N_{So}}{2}\right) \right\} , \qquad (17)$$

which is the expansion of the exact formula for σ_e,

$$\sigma_e = \frac{1}{N_a} \ln \left[\frac{1 - N_{So}}{1 - N_{Si}} \right] , \qquad (18)$$

where N_S is small. Furthermore, the summation $\sum_{\ell=n+1}^{\text{on}} N_{Si}$ was always taken over counters at angles larger than n. Hence, the summation terms could be considered as increasing the small-angle scattering for the following reason: If an antiproton was scattered at a large angle, the chance of it scattering back into one of the small angle counters was small.

The differential-scattering cross section, $\frac{d\sigma}{d\Omega}$, was given by

$$\frac{d\sigma}{d\Omega} = \frac{1}{N_a} \frac{s_{ni} - s_{no}}{\Omega_n} \qquad (19)$$

where Ω_n is the solid angle of the nth counter. If $\frac{d\sigma}{d\Omega}$ is integrated over the total solid angle, the scattering cross section is obtained. Since it was impossible to distinguish the antiproton from the proton, all events were classified according to the angle of the forward-scattered particle. Thus, the angular distributions obtained were the sums of the forward and backward distributions.

The values used for A_n and ϵ_n are given in Table II. It was assumed that they were energy-independent. Values for Ω_n

Table II

Values used in cross section calculations.
Quantities are defined in the text.

	ϵ_n	$1-a_n$	N_{sni}	N_{sno}	Ω_n
S_1	0.98	0.97	0.00937	0.00666	0.0485
S_2	0.99	0.97	0.00671	0.00217	0.0720
S_3	0.99	0.97	0.00584	0.00237	0.0954
S_4	0.99	0.96	0.00500	0.00094	0.1150
R + Q	1.00	0.95	0.02349	0.00158	5.91

and N_{sn} at 0.98 Bev are also given, but the breakdown of the large-angle points is not shown.

D. Charge-Exchange Cross Section

The charge-exchange cross section, σ_{CE}, was given by

$$\sigma_{CE} = \frac{N_{mi} - \sum_{\substack{\text{all} \\ \text{counters}}} N_{sni} (1-\epsilon_n)}{t_{ai}} - \frac{N_{mo} - \sum_{\substack{\text{all} \\ \text{counters}}} N_{sno} (1-\epsilon_n)}{t_{ao}}, \tag{20}$$

where N_m is the fraction of events without any counts in any of the counters. The summation terms correct for scatterings that went between the counters and were counted as misses, and t_a corrects for the fact that if an antiproton underwent annihilation, it could not have charge-exchanged or be detected as such.

E. Uncertainties and Corrections

The main uncertainty in all of the cross sections, with the exception of the charge-exchange cross section, was the statistical uncertainty. There were other sources of errors present, and the uncertainties arising from these errors were compounded with the statistical uncertainty by taking the square root of the sum of the squares of all the uncertainties.

When a particle was scattered at an angle larger than 150 deg in the center of mass, it had a very low energy and was absorbed by the target or surrounding material. If this backward-scattered particle was an antiproton, its absorption would result in its annihilation, and this annihilation could not be distinguished from a normal annihilation. Thus, all antiprotons which were scattered at angles larger than 150 deg could not be detected as such. From a low value of the differential scattering at large angles the correction for this effect was taken to be less than 1mb.

The possibility that some inelastic events were classified as scatterings is small for two reasons. The most important one is that the average number of secondaries from the inelastic events was large and the detection efficiency was high. The other argument depends upon the good angular resolution of our counter system. From the angular distribution of one- and two-particle events that were not classified as scatterings, an estimate was made of the fraction of these events that sent secondaries at just the right angle to simulate a scattering. From the number of inelastic events of this type and the number of elastic scatterings, it was then calculated that less than 5% of the scatterings were inelastic events.

There was an uncertainty in the number of charge-exchanges because of an uncertainty in the number of missed elastic and inelastic events. The estimate of the uncertainty in the number of missed scatterings was obtained by assuming that $(1-\epsilon_n)$ was 50% uncertain. Since the $\underline{a}$ counters counted only particles from inelastic events, it was used to measure an upper limit on the detection efficiency of the system for inelastic events. Any event that sent a particle into $\underline{a}$ also must have sent particle s into the other counter $\underline{s}$ in order to have conserved momentum. By measuring how often these other counters counted, we obtained a measure of the detection efficiency of the system for inelastic events; less than 1% of the inelastic events were misses.

One particular type of event that could have been mistaken for a charge-exchange event is

$$\bar{P} + P \rightarrow \bar{N} + N + \pi^0 , \qquad (21)$$

with the γ-rays from the π^0 coming forward and not going through the lead around the target. From the value for the charged-pion production cross section estimated below and by assuming the neutral pion cross section to be less we estimate that the error from this effect is less than 1 mb.

RESULTS

The results of this experiment are given in Table III. Figures 7 through 11 show these results along with results from other experiments. The cross sections at 0.98 Bev agree reasonably with the high-energy points of Ellioff et al.[8] Each of the different cross sections drops off slowly with increasing energy and approximately with the inverse first power of the velocity, with the exception of the charge-exchange cross section, which remains about the same.

The cross section for production of one charged pion by

$$\bar{P} + P \rightarrow \bar{P} + N + \pi^{+} \qquad (22)$$

or

$$\bar{P} + P \rightarrow \bar{N} + P + \pi^{-} \qquad (23)$$

was estimated to be about 6 mb at each energy. This estimate was obtained from the number of detected one- and two-particle events inconsistent with being a scattering or an annihilation. The cross section could be larger than this estimate, since only events with detected secondaries going into the forward hemisphere were used. Conversely, it could be less, since there could have been other events in which only one or two particles were seen in the forward hemisphere, such as scatterings that annihilated in the counters, annihilations in which all the particles were not seen, and annihilation into two charged pions with both pions coming forward. Considering these effects and the data, we estimate that this cross section might be in error as much as 3 mb in either direction.

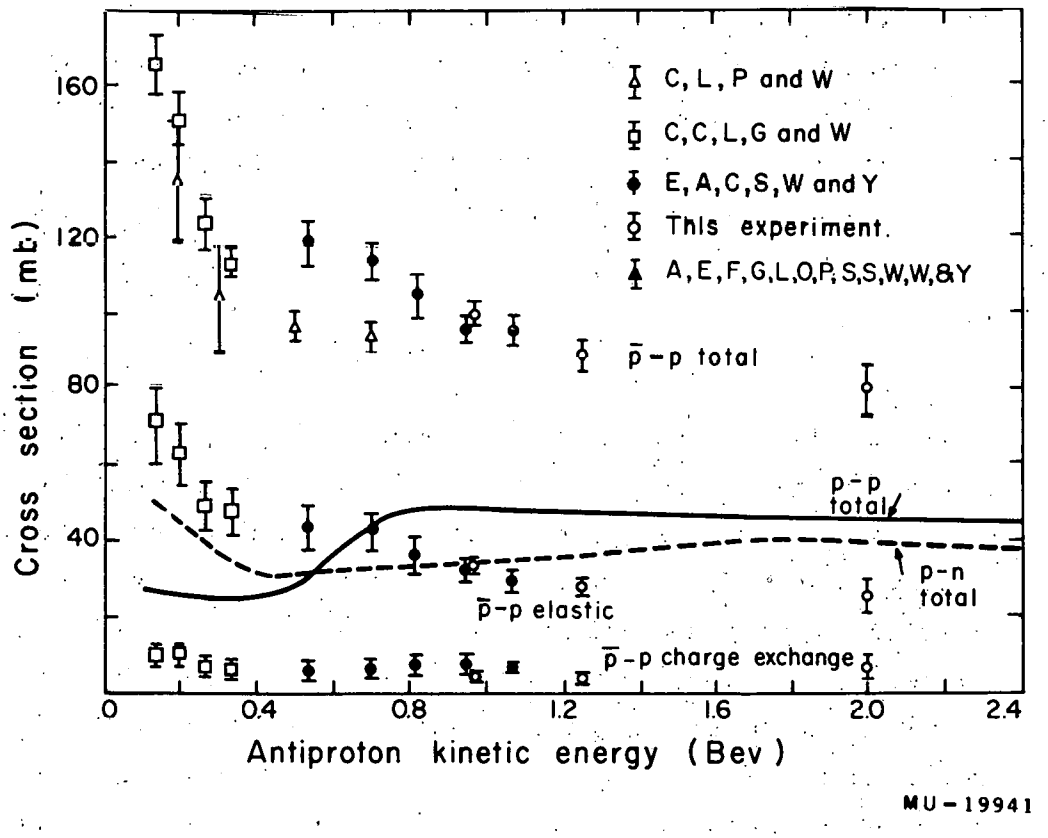

Fig. 7. Energy dependence of total, elastic , and charge-exchange $\bar{p}$-p cross sections. Results of this experiment are indicated by open circles. The solid circles are from reference 8, squares from reference 11, open triangle from reference 6, and solid triangle from reference 9. For comparison, p-p and p-n total cross sections are shown. The uncertainties are both statistical and instrumental in origin.

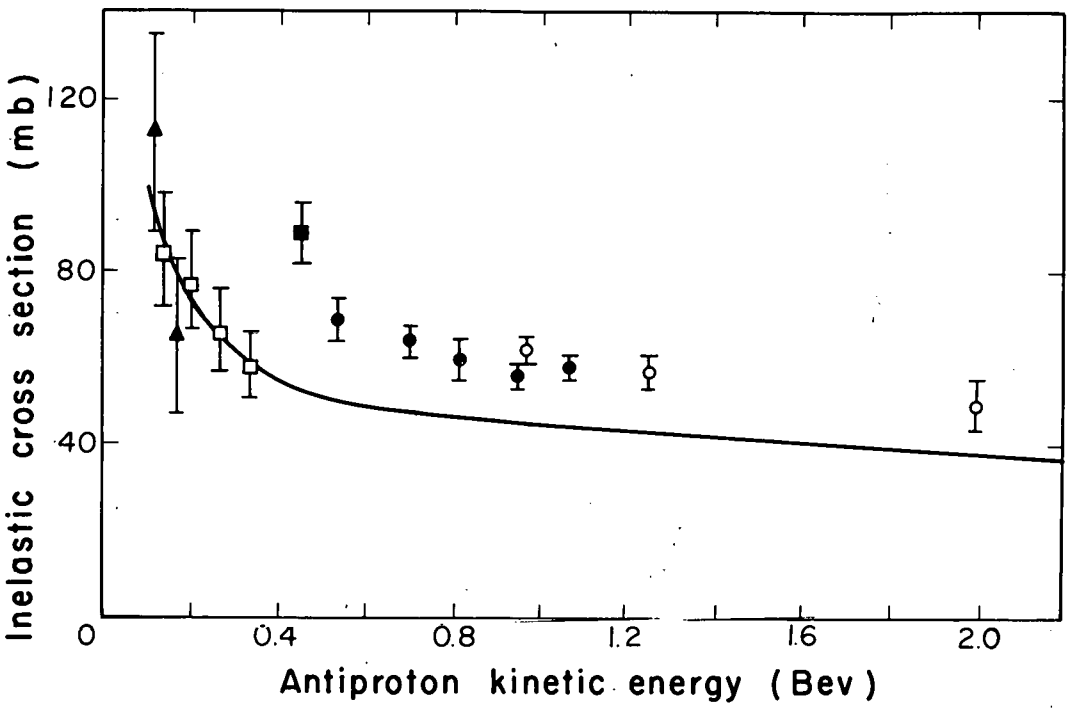

Fig. 8. Energy dependence of inelastic $\bar{p}$-p cross sections. Results of this experiment are indicated by open circles. The solid circles are from reference 8, open squares from reference 11, and the solid triangle from reference 9. The solid square is the annihilation cross section from reference 7. The curve is from the model of Koba and Takeda (reference 14).

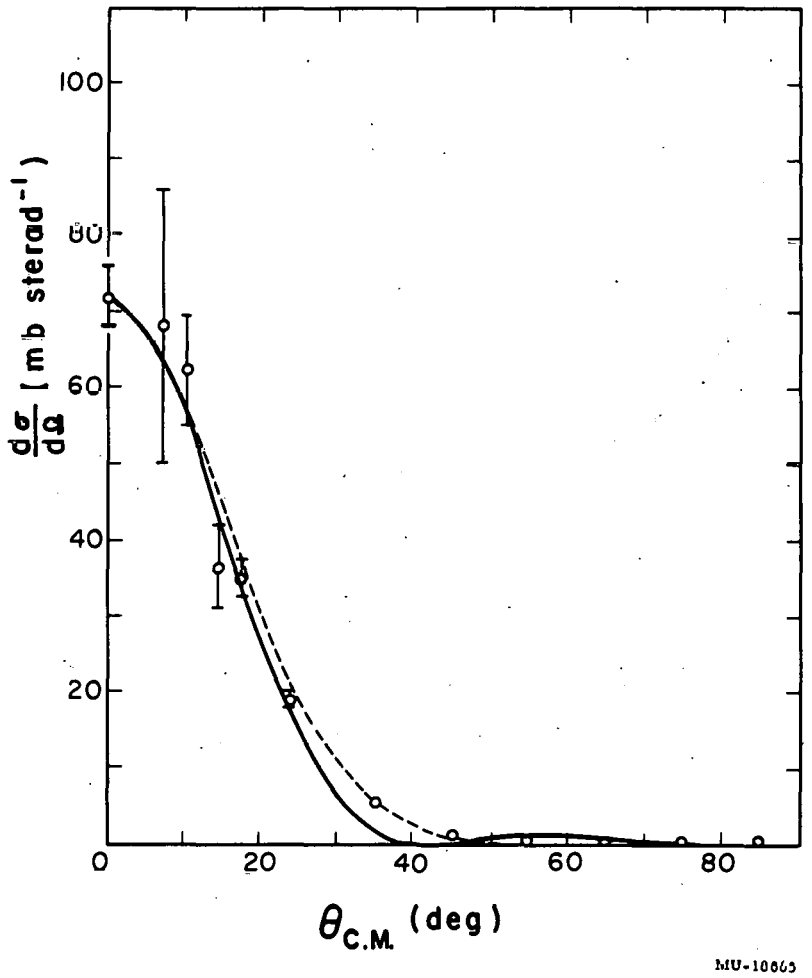

Fig. 9. Angular distributions of the elastic scatterings at 0.98 Bev. The zero-degree point was obtained from the measured total cross section with the help of the optical theorem. It is a minimum value, as is predicted for a purely absorptive interaction. The curves are from an optical-model calculation described in the text. Indicated uncertainties are statistical only.

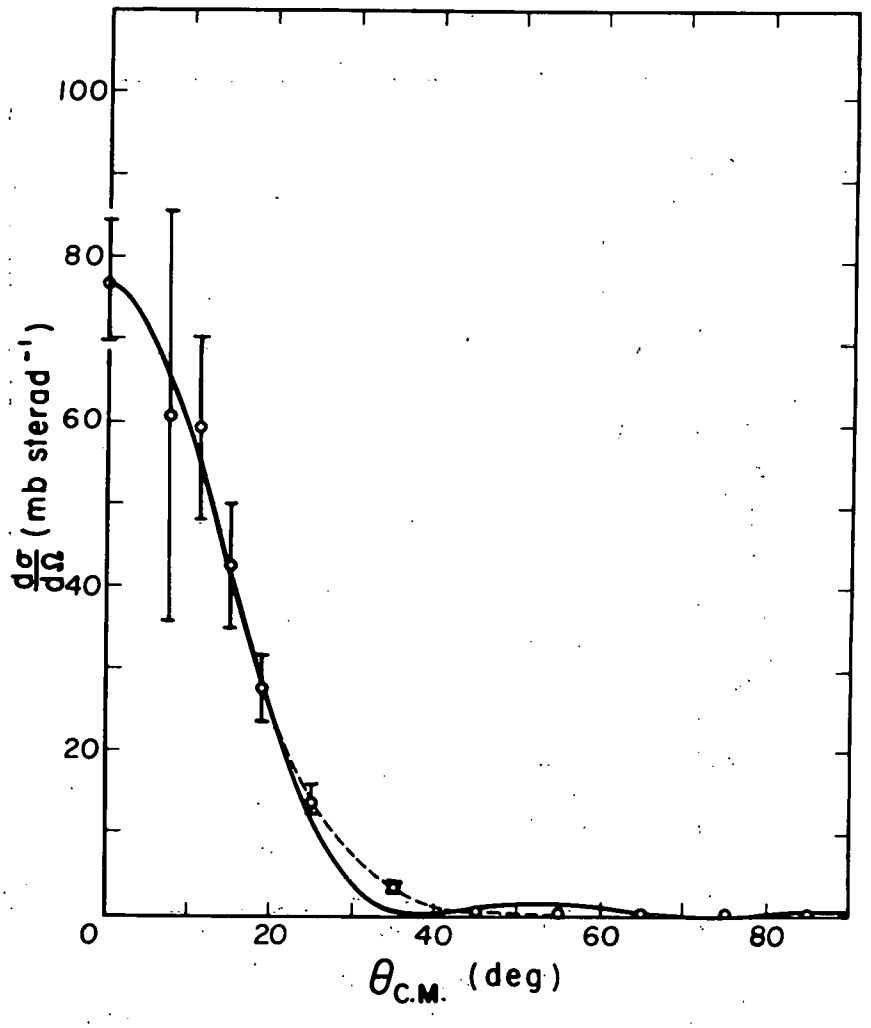

Fig. 10. Angular distribution of the elastic scatterings at 1.25 Bev.

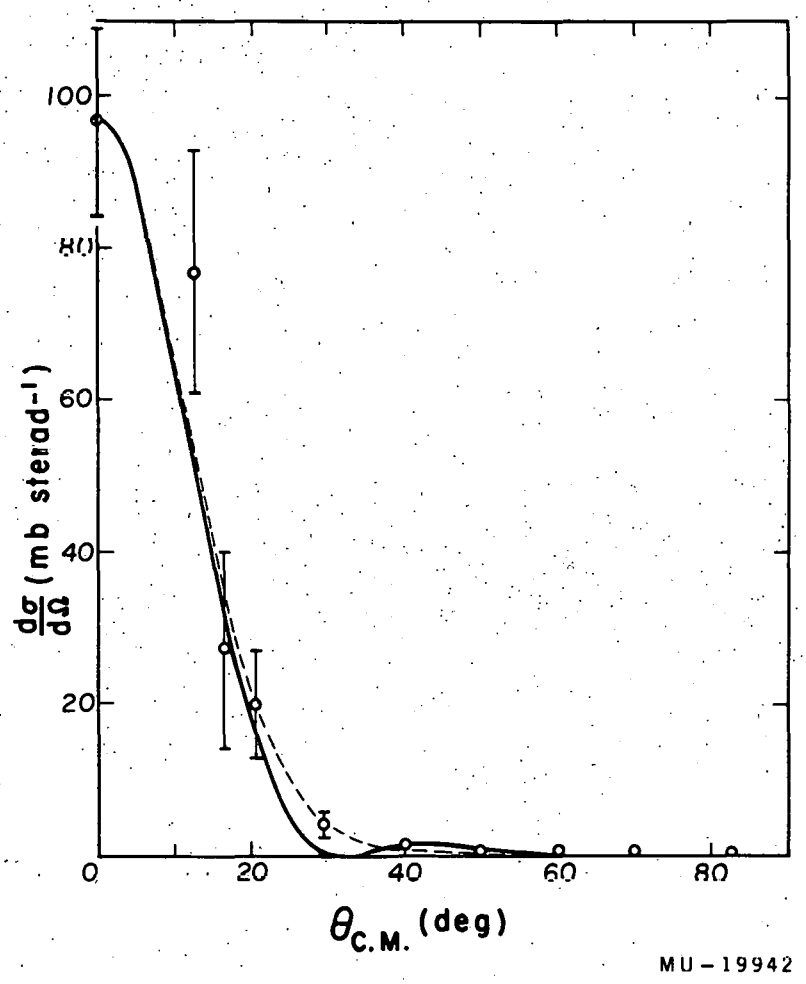

Fig. 11. Angular distribution of the elastic scattering at 2.0 Bev.

Table III

Antiproton-proton cross sections

Kinetic energy (Mev)	Total cross section (mb)	Observed elastic cross section (mb)	Minimum cutoff angle (deg c.m.)	Forward scattering correction (mb)	Corrected elastic cross section (mb)	Charge-exchange cross section (mb)	Inelastic cross section (mb)
0.98	100±3	31	5.4	2	33±2	$5^{+1}_{-1.5}$	62±3
1.25	89±4	26	5.7	2	28±2	4±1	57±4
200	80±6	22	6.3	3	25±4	6^{+2}_{-3}	49±6

OPTICAL MODEL

There is one very noticeable difference between the high-energy data of this experiment and low-energy data. At low energies the inelastic cross section is about the same size as the elastic cross section, while at high energies the inelastic cross section is twice the elastic cross section. Furthermore, the angular distributions at these high energies differ considerably from those obtained at low energies.[11] Because of these differences, it was felt that an optical-model fit to the data would be appropriate.

The optical model of Fernbach, Serber, and Taylor[17] was used to fit the data. In this model the interaction is described in terms of a complex index of refraction, the real part producing the phase shift, and the imaginary part the absorption. For an incident wave of unit amplitude and zero phase shift the amplitude of scattering, $f(\theta)$, into an angle θ is given by

$$f(\theta) = k \int_0^a (1 - a e^{i\phi}) J_0 (k\rho \sin \theta) \rho d\rho \qquad (24)$$

where ρ is the projected distance from the center of the interaction measured on a plane perpendicular to the direction of the incident particle whose wave number is k, J_0 is the zero th-order Bessel function, and a and ϕ are respectively the amplitude and phase shift of the transmitted wave. Both a and ϕ are functions of ρ. The elastic and absorption cross sections are given respectively by

$$\sigma_e = 2\pi \int_0^a \left| 1 - a e^{\phi} \right|^2 \rho d\rho \qquad (25)$$

and

$$\sigma_a = 2\pi \int_0^a (1 - a^2) \rho d\rho . \qquad (26)$$

These equations are most easily solved by using the black-or gray-disk models. Here, it is assumed that $\phi = 0$ and a is a constant, a_0, out to some radius R and is unity from R out to infinity. This

model corresponds to a disk of radius R that absorbs $(1-a_0^2)$ of the particles passing through it. It is said to be a black disk if the total absorption of particles hitting the disk, a_0, is zero. For this model, Eqs. (24) through (26) reduce to

$$f(\theta) = kR^2 \frac{J_1(kR\sin\theta)}{kR\sin\theta}, \tag{27}$$

$$\sigma_e = (1-a_0)^2 \pi R^2, \tag{28}$$

and

$$\sigma_a = (1-a_0^2)\pi R^2, \tag{29}$$

where J_1 is the first-order Bessel function. The solid curves in Figs. 9, 10, and 11 are a fit to the data by this model, using the value of the parameters given in Table IV. Here a_0 and R were determined by the values σ_e and σ_a rather than by finding the best fit to the angular distribution. The value used for σ_c was the sum of the inelastic and charge-exchange cross sections; thus, the zero degree point had to be the same as obtained from the total cross section. Sin θ was replaced by 2 sin $\theta/2$ in the calculations.[18] One reason is that 2 k R sin $\theta/2$ always seems to fit the data better. Another reason is for small angles 2 k R sin $\theta/2$ reduces to k R sin θ so there isn't any change, and for large angles where the theory is not as good, 2 k sin $\theta/2$ is a better parameter as it represents the momentum transfer, the quantity used in most theories.

From the solid curves in Figs. 9, 10, and 11, one can see that although the gray disk fits the small-angle points, it gives too sharp a cut-off. If a small amount of phase shift is added ($\phi \neq 0$), a better fit can be obtained. For a good fit, the phase shift would have to be such that it produced only a fraction of a millibarn of scattering at large angles and about 3 to 5 mb at angles about the minimums in the gray-disk curves and smaller angles. It does not seem likely that the real scattering would have an angular distribution like this.

The model that was used to obtain a good fit to the data was that of a perfectly black disk ($a = 0$) of radius R surrounded by a structure whose opacity falls off as a gaussian. This model can be expressed in terms of a and ϕ by

$$\phi = 0, \; a = 0, \; 0 < \rho \leq R_0 \tag{30}$$

$$\phi = 0, \; (1-a) = \exp\left[\frac{-(e^2 - R_0^2)}{\rho_0^2}\right] e \geq R_0 \tag{31}$$

This model corresponds to a nucleon with a black (absorbing) core surrounded by a pion cloud that does not produce a phase shift and has an interaction density that drops off exponentially with the distance from the core. The cross sections are then given by placing conditions (30) and (31) into Eqs. (24) and (26) and integrating:

$$\sigma_e = \pi R_0^2 + \frac{1}{2} \pi \rho_0^2 \tag{32}$$

$$\sigma_a = \pi R_0^2 + \frac{3}{2} \pi \rho_0^2 . \tag{33}$$

The values of ρ_0 and R_0 obtained using this method are given in Table IV. From these values for ρ_0 and R_0, $f(\theta)$ was calculated for the different energies, and the resulting distribution is shown as the dashed curve in Figs. 9, 10, and 11.

For this model, the expression for $f(\theta)$ can be broken up into two parts,

$$f(\theta) = f(\theta)_I + f(\theta)_{II} . \tag{34}$$

One part comes from the black disk,

$$f(\theta)_I = k \int_0^{R_0} J_0 (k \rho \sin \theta) \, \rho d\rho \tag{35}$$

$$= k R^2 \frac{J_1 (k R \sin \theta)}{k R \sin \theta} , \tag{36}$$

Table IV

Values used for parameters in the optical-model calculations. The errors are derived from the errors in the scattering cross section.

Kinetic energy (Mev)	a_0	R (10^{-13} cm)	R_0 (10^{-13} cm)	ρ_0 (10^{-13} cm)
0.98	0.34±.03	1.55±.02	0.73±.06	1.03±.03
1.25	0.37±.03	1.50±.02	0.61±.08	1.02±.03
2.00	0.38±.07	1.43±.04	0.57±.17	0.98±.07

and one comes from the surrounding cloud,

$$f(\theta)_{II} = k \int_{R_0}^{a} J_0 (k \rho \sin \theta) \exp\left[\frac{-(\rho^2 - R_0^2)}{\rho_0^2}\right] \rho d\rho . \tag{37}$$

To be able to integrate Eq. (37), we replace $J_0 (k \rho \sin \theta)$ by its infinite-series expansion (the method used here is taken from the method used in Watson for a similar integral[19]). Thus, we have

$$f(2)_{II} = k \exp\left(\frac{R_0}{\rho_0}\right)^2 \sum \frac{(-1)^m \left(\frac{1}{2} k \sin \theta\right)^{2m}}{m!\ \Gamma (m+1)} \int_{R_0}^{a} \rho^{2m+1} \exp-\left(\frac{\rho}{\rho_0}\right)^2 d\rho . \tag{38}$$

After integrating by parts, one obtains

$$f(\theta)_{II} = \frac{1}{2} k \rho_0^2 \exp\left(\frac{R}{\rho_0}\right)^2 \sum_{m=0}^{\infty} \frac{(-1)^m}{m!} \left(\frac{1}{2} k \rho_0 \sin \theta\right)^{2m} \sum_{n=0}^{m} \frac{1}{n!} \left(\frac{R_0}{\rho_0}\right)^{2n} , \tag{39}$$

which reduces to

$$f(\theta) = \frac{1}{2} k \rho_0^2 \exp - \left(\frac{1}{2} k \rho_0 \sin \theta\right)^2 \tag{40}$$

for the case where R_0 is zero, with no hard core. Equation (39) can be regrouped and written as

$$f(e)_{II} = \frac{1}{2} k \rho_0^2 \left\{ \exp\left[-(1/2 k \rho_0 \sin \theta)^2 + \left(\frac{R_0}{\rho_0}\right)^2\right] - \sum_{n=1}^{\infty} \frac{1}{n!} \left(\frac{R_0}{\rho_0}\right)^{an} \left[\sum_{\ell=0}^{n-1} \frac{(-1)^\ell}{\ell!} (k \rho_0 \sin \theta)^{2\ell}\right] \right. \tag{41}$$

For small values of θ and for cases with $R_0 < \rho_0$, the series in Eq. (40) converges rapidly, and only a small number of terms need be considered. Even at large angles, only three or four terms had to be considered at 1.0 Bev and 1.25 Bev, while at 2.0 Bev seven terms were used. The value of the differential-scattering cross section at large angles was never larger than a few tenths of a millibarn, and since it was so small, it was not plotted in Figs. 9, 10 and 11. In the calculations, $\sin\theta$ was replaced by $2 \sin\theta/2$ for the same reasons as mentioned before.

An exponential fall with the first power of the distance might be thought of as theoretically more appropriate than that of the second power used above, since the first power is used in the Yukawa potential. It was not used here for two reasons. One is that the value of the fall-off parameter used in the Yukawa potential does not give a good fit to the elastic and inelastic cross sections; it is a factor of 3 or 4 larger than the value needed to obtain a good fit. The other reason is that the calculations of the angular distributions were much more difficult. The above method could not be used, because the series obtained by using this method did not converge very rapidly.

CONCLUSIONS

A model of a black disk surrounded by a structure whose opacity falls off exponentially with the projected distance from the disk seems to fit the data fairly well. Since the parameters involved were determined by the elastic and inelastic cross sections, the only restriction placed on the angular distribution was that it should add up to the total elastic cross section. Thus, the good fit is more significant than that of one made by varying several parameters until a fit is obtained. By adding a small amount of phase shift (about 3 or 4 deg) the calculated scattering could have been made to fit the data at large angles without appreciably changing the angular distribution at small angles. It should be pointed out that these distributions are considerably different from those at lower energies. In the energy range of 133 to 333 Mev, it was found that the angular distributions could be fitted by a perfectly black disc.[11] At 500 Mev, it was also found that the angular distribution could be fitted by a black disk.[20]

The change from a totally absorbing type of interaction at lower energies to a partially absorbing interaction at energies used in this experiment is not only shown by the angular distribution but also by the ratio of inelastic to elastic cross sections. A total absorbing interaction gives a one-to-one ratio of inelastic to elastic which should be compared to the ratio of two-to-one found in this experiment. One possible reason for this effect is that at low energies any antiproton that comes within the range of the pion exchange force is drawn into the core and is annihilated, while at high energies the force does not always act long enough to draw the antiproton into the core.

A model that gives fair agreement with the annihilation cross section is the model of Koba and Takeda.[14] They considered the nucleon to be made up of two parts--an absorbing core surrounded by a pion cloud--and considered that an antiproton and proton annihilate whenever their cores touch. In this model, the radius of interaction is made larger because of partial absorption of each of the

partial waves, an effect that can be interpreted as extending the distance that an antiproton can be from a proton and still annihilate with it. The range to which it can reach is determined by the wave length of the antiproton in the center of mass $\lambda\!\!\!^{-}$ and the radius of the core, R_0. The absorption cross section, σ_a, is then given by

$$\sigma_a = \pi (R_0 + \lambda\!\!\!^{-})^2 \quad . \tag{42}$$

The solid curve in Fig. 8 is a plot of Eq. (42) for $R_0 = 0.9 \times 10^{-13}$ cm. The high-energy points may be above the curve because of pion production (inelastic scatterings), which this theory does not take into account. Thus, in order for the theory to fit the data, the pion production cross section must be about 10 to 15 mb. A point in favor of this argument is that it gives a production cross section that is constant with energy, a characteristic that is common to the proton-proton and proton-neutron interaction.

At high energies there is a general lack of theories to which the results can be compared. One of the reasons is the difficulty involved in any calculation at high energies because of the large number of partial waves that need to be considered. Methods like that of the "Optical Model", which averages over all the partial waves, must be used.

The most noticeable characteristics about the cross sections are the large radius needed to fit them and the slow rate at which they are dropping off with increasing energy. At high energies the annihilation cross section should approach the size of the core that is expected to have a radius equal to the Compton wave length of the proton. The radii determined by the optical-model calculations are much larger than the Compton wave length of the proton (about 0.2×10^{-13} cm). Large values for the nucleon radius have been observed in other experiments. A radius of about 0.8×10^{-13} cm was found in electron-proton scattering.[21] Measurements with high energy protons[22, 23] and pions[24–27] give a similar size.

ACKNOWLEDGMENTS

This experiment was performed with the aid and cooperation of many people. In particular I would like to thank Dr. Rafael Armenterous for his help during the experiment, for his help in reducing the data, and for his advice on the writing of this thesis. Also, I would like to thank Messrs. Bruce Cork and Glen Lambertson, and Dr. William Wenzel for their help and guidance throughout this experiment and for their assistance throughout the author's graduate work.

For their help in the many different phases of this experiment, I would like to express my appreciation to the laboratory technicians: Max J. Aiken, Carl Burton, Dick Crolius, Ralph Duncan, Larry Gilboy, Gene Rosa, and Ching Lin Wong. The help of Carl Noble in reducing the data is gratefully acknowledged.

Finally I would like to thank the Bevatron crew for the operation of the Bevatron.

This work was done under the auspices of the U. S. Atomic Energy Commission.

REFERENCES

1. Chamberlain, Segrè, Wiegand, and Ypsilantis, Phys. Rev. 100, 947 (1955).
2. Chamberlain, Keller, Segrè, Steiner, Wiegand, and Ypsilantis, Phys. Rev. 102, 1637 (1956).
3. Chamberlain, Chupp, Ekspong, Goldhaber, Goldhaber, Lofgren, Segrè, Wiegand, Amaldi, Baroni, Castagnoli, Franzinetti, and Manfredini, Phys. Rev. 102, 921 (1956).
4. Barkas, Birge, Chupp, Ekspong, Goldhaber, Goldhaber, Heckman Perkins, Sandweiss, Segrè, Smith, Stork, Van Rossum, Amaldi, Baroni, Castagnoli, Franzinetti, and Manfredini, Phys. Rev. 105, 1037 (1957).
5. Brabant, Cork, Horwitz, Moyer, Murray, Wallace, and Wenzel, Phys. Rev. 101, 498 (1956) and ibid. 102, 1622 (1956).
6. Cork, Lambertson, Piccioni, and Wenzel, Phys. Rev. 107, 248 (1957).
7. Chamberlain, Keller, Mermod, Segrè, Steiner, and Ypsilantis, Phys. Rev. 108, 1553 (1957).
8. Elioff, Agnew, Chamberlain, Steiner, Wiegand, and Ypsilantis, Phys. Rev. Letters 3, 285 (1959).
9. Agnew, Elioff, Fowler, Gilly, Lander, Oswald, Powell, Segrè Steiner, White, Wiegand, and Ypsilantis, Antiproton Interactions in Propane Below 200 Mev, UCRL-8822, June 1959.
10. Goldhaber, Kalogeropoulos, and Silberberg, Phys. Rev. 110, 1474 (1958).
11. Coombes, Cork, Galbraith, Lambertson, and Wenzel, Phys. Rev. 112, 1303 (1958).
12. J. S. Ball and G. F. Chew, Phys. Rev. 109, 1395 (1959).
13. Jose R. Fulco, Phys. Rev. 110, 784 (1958).
14. Z. Koba and G. Takeda, Progr. Theoret. Phys. (Kyoto) 19, 269 (1958).

15. Chamberlain, Chupp, Goldhaber, Segrè, Wiegand, Amaldi, Baroni Castagnoli, Franzinetti, and Manfredini, Nuovo cimento 3, 447 (1956).
16. L. D. Landau and E. M. Lifshilz, Quantum Mechanics (Addison-Wesley Publishing Co., Inc., Reading, Mass., 1958), p. 398.
17. Fernbach, Serber, and Taylor, Phys. Rev. 75, 1352 (1949).
18. R. J. Glauber, Lectures in Theoretical Physics (Interscience Publishers, New York, N. Y., 1959), p. 345.
19. G. N. Watson, Theory of Bessel Functions (Cambridge University Press, Cambridge, 1952), p. 393.
20. S. Goldhaber, W. B. Fowler, G. Goldhaber, T. F. Hoang, W. M. Powell, and R. Silberberg, Bull. Am. Phys. Soc., Ser. II, 4, 368 (1959).
21. E. E. Chambers and R. Hostadter, Phys. Rev. 103, 1454 (1956).
22. W. Rarita, Phys. Rev. 104, 221 (1956).
23. Cork, Wenzel, and Causey, Phys. Rev. 107, 859 (1957).
24. Cronin, Cool, and Abashian, Phys. Rev. 107, 1121 (1957).
25. Walker, Hushfar, and Shephard, Phys. Rev. 104, 526 (1956).
26. Cool, Piccioni, and Clark, Phys. Rev. 103, 1082 (1956).
27. Maenchen, Powell, Saphir, and Wright, Phys. Rev. 99, 1619 (1955).